Chaos, Solitons and Fractals 185 (2024) 115088

Contents lists available at ScienceDirect

Chaos, Solitons and Fractals

journal homepage: www.elsevier.com/locate/chaos

Heat-transfer fingerprint of Josephson breathers

Duilio De Santis [a,*], Bernardo Spagnolo [a,b], Angelo Carollo [a], Davide Valenti [a], Claudio Guarcello [c,d]

[a] Dipartimento di Fisica e Chimica "E. Segrè", Group of Interdisciplinary Theoretical Physics, Università degli Studi di Palermo, I-90128, Palermo, Italy
[b] Radiophysics Department, Lobachevsky State University, 603950, Nizhniy Novgorod, Russia
[c] Dipartimento di Fisica "E. R. Caianiello", Università degli Studi di Salerno, I-84084, Fisciano, Salerno, Italy
[d] INFN, Sezione di Napoli, Gruppo Collegato di Salerno - Complesso Universitario di Monte S. Angelo, I-80126, Napoli, Italy

ARTICLE INFO

Keywords:
Solitons
Breathers
Long Josephson junctions
Thermally biased junctions
Coherent caloritronics

ABSTRACT

A sine–Gordon breather is demonstrated to enhance the heat transfer in a thermally biased long Josephson junction. This solitonic channel allows for the tailoring of the local temperature throughout the system. Furthermore, the phenomenon implies a clear thermal fingerprint for the breather, and thus a 'non-destructive' breather detection strategy is proposed here. Distinct breathing frequencies result in morphologically different local temperature peaks, which can be identified in an experiment.

1. Introduction

The soaring development of quantum technologies continuously propels the field of thermodynamics towards new fundamental and applied challenges, such as the accurate heat management at the nanoscale [1–3]. This is the goal of *caloritronics* [4–6], whose interest has been revived after the recent experimental demonstration of the phase-coherent control of the thermal transport in Josephson devices [7,8]. Superconducting phase coherence offers a unique knob for mastering heat flows. This feature has led researchers to conceive and implement nonlinear caloritronic devices for different applications, such as thermometry [9–12] and refrigeration [13–17], memories [18,19] and engines [20,21], routers [22–24] and switches [25], diffractors [26] and radiation detectors [27,28]. The strength of *phase-coherent caloritronics* lies in the feasibility of adjusting the temperature by controlling the Josephson phase, *e.g.*, via externally applied magnetic fields.

Extended Josephson systems, such as long Josephson junctions (LJJs) [29], constitute an established research topic in applied superconductivity, thanks to their richness in terms of both physical phenomena and cutting-edge applications [30–35]. From the viewpoint of thermal transport, the behavior of these devices is, however, largely unknown [36–38]. It is then important to ask: can heat flows represent a new paradigm in such a context? Can this provide unprecedented means to experimentally investigate complex scenarios which have remained beyond reach for many years?

We answer these questions by focusing on Josephson breathers, *i.e.*, kink–antikink (or fluxon–antifluxon) oscillating bound states [39,40]. Such excitations have long been sought after, and extensive investigations in standard (thermally unbiased) LJJs have not succeeded in finding any direct experimental signature [41–47]. Here we propose to consider breathers from a new perspective, that of thermal transport. A first, notable achievement of the present paper is showing that a breather alters the heat transfer in thermally biased junctions. The mastering of the local temperature[1] within the system can thus be achieved via breathers, an intriguing fact which enhances their physical relevance. In addition, this unveiled property naturally sets the stage for a long sought non-destructive breather detection scheme, *i.e.*, a protocol not involving the mode's breakup. Morphologically different local thermal profiles are found at distinct oscillation frequencies. The latter fact is useful in view of experiments and is a consequence of the analytical sine–Gordon (SG) breather waveform. By exploiting noise and ac driving for the excitation and the stabilization of the nonlinear breathing states [46,47], the robustness of the thermal fingerprint is demonstrated as well. In other words, the below proposal outlines, under realistic conditions, the key steps for successfully observing breathers in laboratory.

The achievement of the Josephson breather's detection paves the way for several applications in, *e.g.*, information and communication technology [43,44], generation of THz radiation [41,48], and quantum technology [49,50], whose practical implementation has been limited, so far, by the lack of experimental evidence on this solitonic

* Corresponding author.
E-mail address: duilio.desantis@unipa.it (D. De Santis).

[1] In cryogenic devices, electron and phonon subsystems can have different temperatures [1]. Here, the phonon temperature is examined.

https://doi.org/10.1016/j.chaos.2024.115088
Received 26 April 2024; Received in revised form 27 May 2024; Accepted 28 May 2024
Available online 24 June 2024
0960-0779/© 2024 The Authors. Published by Elsevier Ltd. This is an open access article under the CC BY license (http://creativecommons.org/licenses/by/4.0/).

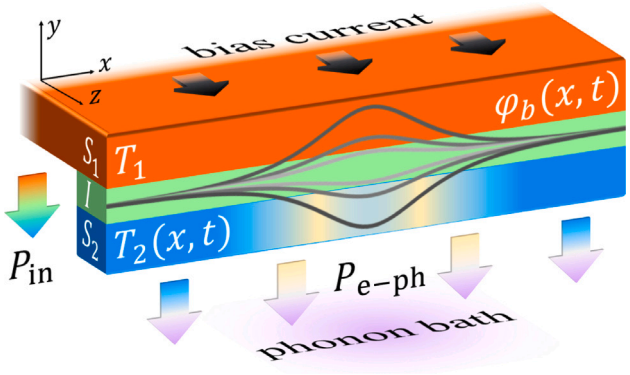

Fig. 1. Pictorial view of an overlap-geometry, current-driven LJJ, in the presence of a thermal bias. The temperature T_1 of the first electrode (S_1) is fixed, whereas S_2 has a floating temperature $T_2(x,t)$. The latter electrode is also in thermal contact with a phonon bath at temperature T_b. For $T_1 > T_2(x,t) \geq T_b$, the thermal power $P_{\rm in}(T_1,T_2,\varphi,V)$ coming into S_2 is depicted, along with the outgoing term $P_{\rm e-ph}(T_2,T_b)$, which is due to S_2's quasiparticles coupling with the lattice phonons at T_b. Lastly, the drawing illustrates the double-peaked local heating in S_2 caused by the breather oscillations, quantitatively discussed below.

state. Moreover, the LJJ and the SG framework represent very popular testbeds for a plethora of nonlinear science studies [30,39,40,51,52]. Probing fundamental modes such as SG breathers is therefore a pressing issue that brings together many different research areas, including biology [53], high-T_c superconductivity [54,55], geology [56,57], and optics [58,59]. On the quantum side, the SG theory and its breather excitations constitute a matter of ever-growing interest, see Refs. [60–66] and references therein.

The paper has the following structure. Section 2 is concerned with the model. In the first part of Section 3 (*i.e.*, "Breather-enhanced thermal transport"), results of simulations starting from analytical breather initial conditions are discussed in detail to illustrate how the exact breather waveforms project onto the thermal realm. The rest of Section 3 (*i.e.*, "Detection proposal") shows how one can nucleate a breather from a realistic (uniform) initial condition, while also demonstrating the robustness of its thermal signature. Finally, conclusions are drawn in Section 4.

2. The model

The dynamics of the LJJ is described via the perturbed SG equation for the Josephson phase $\varphi(\mathcal{X},\mathcal{T})$ [29]

$$\frac{\partial^2\varphi}{\partial\mathcal{X}^2} - \frac{\partial^2\varphi}{\partial\mathcal{T}^2} - \alpha\frac{\partial\varphi}{\partial\mathcal{T}} = \sin\varphi - \eta\sin[\omega(\mathcal{T}-\mathcal{T}_0)] - \gamma_n(\mathcal{X},\mathcal{T}), \tag{1}$$

which is written in terms of dimensionless space and time variables, *i.e.*, $\mathcal{X} = x/\lambda_J$ and $\mathcal{T} = t\omega_p$. Here, the characteristic scales are given by the Josephson penetration depth $\lambda_J = \sqrt{\Phi_0/\left(2\pi\mu_0 t_d J_c\right)}$ and the Josephson plasma frequency $\omega_p = \sqrt{2\pi J_c/\left(\Phi_0 C\right)}$ [29], where t_d is the effective magnetic thickness, $J_c = I_c/A$ the Josephson critical current per unit area [with $A = L\times W$ being the junction's area, and L (W) its length (width)], and C the junction's specific capacitance (Φ_0 and μ_0 are the magnetic flux quantum and the vacuum permeability, respectively). Furthermore, in Eq. (1), $\alpha = 1/\left(\omega_p R_a C\right)$ is the damping coefficient (where R_a indicates the normal resistance per area), ω (η) is the frequency (amplitude) of the external ac driving in units of ω_p (I_c), $\mathcal{T}_0$ is a normalized time displacement, and $\gamma_n(\mathcal{X},\mathcal{T})$ is a dimensionless noise current with zero average and autocorrelation function given by

$$\langle\gamma_n(\mathcal{X}_1,\mathcal{T}_1)\gamma_n(\mathcal{X}_2,\mathcal{T}_2)\rangle = 2\alpha\Gamma\delta(\mathcal{X}_1-\mathcal{X}_2)\delta(\mathcal{T}_1-\mathcal{T}_2). \tag{2}$$

The noise strength $\Gamma = 2\pi\mathcal{L}k_BT/\left(\Phi_0 I_c\right)$ is proportional to the normalized junction length $\mathcal{L} = L/\lambda_J$ and the absolute temperature T (k_B is the Boltzmann constant). For an overlap-geometry LJJ, see Fig. 1, and null external magnetic fields, the imposed boundary conditions are $(\partial\varphi/\partial\mathcal{X})\,|_{\mathcal{X}=0,\mathcal{L}} = 0$.

Fig. 1 presents a sketch of the temperature-biased setup examined here, as well as the double-peaked local heating due to the breather oscillations. Specifically, the temperature T_1 of the first electrode (S_1) is fixed, while S_2 has a floating temperature $T_2(x,t)$.[2] The latter electrode is also in thermal contact with a phonon bath at known temperature T_b, and the relation $T_1 > T_2(x,t) \geq T_b$ holds. The spatio-temporal behavior of the floating temperature is modeled by the diffusion equation [36,67,68]

$$\frac{\partial}{\partial x}\left[\kappa(T_2)\frac{\partial T_2}{\partial x}\right] + \mathcal{P}_{\rm tot}(T_1,T_2,T_b,\varphi,V) = c_v(T_2)\frac{\partial T_2}{\partial t}, \tag{3}$$

where $\kappa(T_2)$ denotes the inhomogeneous electronic heat conductivity, $\mathcal{P}_{\rm tot}(T_1,T_2,T_b,\varphi,V) = \mathcal{P}_{\rm in}(T_1,T_2,\varphi,V) - \mathcal{P}_{\rm e-ph}(T_2,T_b)$, with $\mathcal{P}_{\rm in}(T_1,T_2,\varphi,V)$ and $\mathcal{P}_{\rm e-ph}(T_2,T_b)$ being, respectively, the ingoing and outgoing thermal power densities in S_2 [$V \equiv V(x,t)$ is the voltage drop], see Fig. 1, and $c_v(T_2)$ is the volume-specific heat capacity. Note that the LHS of Eq. (3) describes the heat's spatial diffusion, while its RHS represents the variation of S_2's internal energy.

The phase-dependent 'in' thermal power density is structured as follows [38]

$$\mathcal{P}_{\rm in}(T_1,T_2,\varphi,V) = \mathcal{P}_{\rm qp}(T_1,T_2,V) - \cos\varphi\,\mathcal{P}_{\cos}(T_1,T_2,V). \tag{4}$$

Here, the 'qp' term is a quasiparticle contribution, *i.e.*, it amounts to an S_1 (hot) $\rightarrow$ S_2 (cold) incoherent energy flow, whereas the 'cos' term stems from the energy-carrying tunneling events involving the destruction and recombination of Cooper pairs in both S_1 and S_2 [69,70].

The initial condition for Eq. (3) is $T_2|_{t=0} = T_b$, and the edges of the device are assumed to be thermally isolated, implying $\left(\partial T_2/\partial x\right)|_{x=0,L} = 0$.

Detailed information regarding all the above expressions, including their physical significance and the numerical means to handle them, is given in Appendices A and B. In what follows, an LJJ composed by Nb/AlO_x/Nb is considered, with $L = 300$ μm, $W = 0.5$ μm, $d_2 = 0.1$ μm (thickness of S_2), $d = 1$ nm (thickness of the insulating layer), $R_a = 50\ \Omega\ \mu m^2$, and $C = 100$ fF μm^{-2}. Such a device is thermally biased by setting $T_1 = 7$ K and $T_b = 4.2$ K [36]. As shown in Appendix C, by accounting for the temperature dependence in both $t_d(T_1,T_2)$ and $I_c(T_1,T_2)$, one can estimate the values[3] $\lambda_J \approx 8$ μm (thus $\mathcal{L} = L/\lambda_J \approx 37$), $\omega_p \approx 0.95$ THz, $\alpha \approx 0.2$, and $\Gamma \approx 0.0026$.[4] Before proceeding, it should be also stressed that the overall features found below apply to a wide range of parameter values. The currently chosen set is just meant to provide a realistic example.

3. Results

Breather-enhanced thermal transport. The effects of breathers on the evolution of the temperature $T_2(\mathcal{X},\mathcal{T})$ are studied in the following way. First, the electrode S_2 is allowed to fully thermalize in the absence of excitations, *e.g.*, by taking $\varphi(\mathcal{X},\mathcal{T}<\mathcal{T}_0)$ in an unperturbed scenario. Eq. (1) is then solved for $\mathcal{T}_0 \leq \mathcal{T} \leq \mathcal{T}_f$, and the generation of a stabilized breather centered at $\mathcal{X} = \mathcal{X}_0$ is mimicked by imposing $\varphi|_{\mathcal{T}=\mathcal{T}_0} = \varphi^0|_{\mathcal{T}=\mathcal{T}_0}$ and $(\partial\varphi/\partial\mathcal{T})\,|_{\mathcal{T}=\mathcal{T}_0} = \left(\partial\varphi^0/\partial\mathcal{T}\right)|_{\mathcal{T}=\mathcal{T}_0}$, with $\varphi^0(\mathcal{X},\mathcal{T}) = \varphi_b(\mathcal{X},\mathcal{T}) + \varphi_v(\mathcal{T})$ being the 'breather plus vacuum' state [71]

$$\varphi^0(\mathcal{X},\mathcal{T}) = 4\,\mathrm{atan}\left\{\frac{\sqrt{1-\omega^2}}{\omega}\frac{\cos\left[\omega\left(\mathcal{T}-\mathcal{T}_0\right)+\pi-2\theta\right]}{\cosh\left[\sqrt{1-\omega^2}\left(\mathcal{X}-\mathcal{X}_0\right)\right]}\right\} +$$

[2] This can be achieved via optimization of the electrodes' volumes [36,38].

[3] The approximation $T_2 = T_b$ is made here, since T_2's variations (discussed later in the work) are negligible for the sake of these calculations.

[4] The latter quantity explicitly depends on the temperature T, see Eq. (2). To display the results' robustness even in the 'worst-case' noise scenario, the highest temperature within the system, *i.e.*, $T = T_1$, is taken.

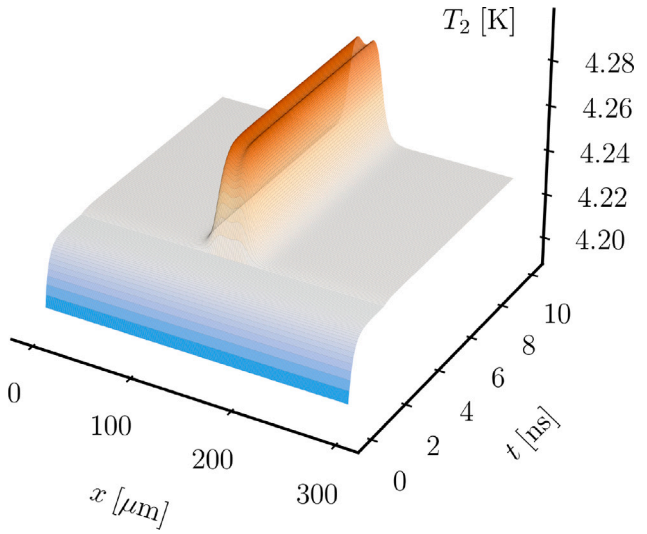

Fig. 2. Spatio-temporal view of the temperature T_2. The generation of a stabilized breather centered at $x_0 = 150$ μm is mimicked at $t_0 = 2$ ns, that is, after S_2 has thermalized at the steady value of ~ 4.23 K. The plot displays the double-peaked local heating, with $\max\{T_2\} \gtrsim 4.27$ K, caused by the breather. Parameter values: $\omega = 0.5$, $\eta = 0.33$, and $\Gamma = 0$.

$$+ \frac{\eta \sin\left[\omega\left(\mathcal{T} - \mathcal{T}_0\right) - \theta\right]}{\sqrt{(1-\omega^2)^2 + \alpha^2\omega^2}}, \quad \tan\theta = \frac{\alpha\omega}{1-\omega^2}, \tag{5}$$

which is known to lock to an ac force of suitable amplitude, *i.e.*, for $\eta \approx \eta_{\rm th}(\omega) = \frac{2\alpha(1-\omega^2)\,\mathrm{asin}\sqrt{1-\omega^2}}{K(1-\omega^2)-E(1-\omega^2)}$ (K and E are, respectively, complete elliptic integrals of the first and the second kind) [71]. The choices $x_0 = \mathcal{X}_0\lambda_J = 150$ μm, $t_0 = \mathcal{T}_0/\omega_p = 2$ ns, and $t_f = \mathcal{T}_f/\omega_p = 10$ ns are made. It is worth adding that the below long-time temperature behaviors do not depend on the value of the excitation-free thermalization time t_0.

Setting $\Gamma = 0$, a typical simulation outcome for $T_2(x,t)$ is shown in Fig. 2 for $\omega = 0.5$ and $\eta = 0.33 \approx \eta_{\rm th}(\omega = 0.5)$. One can first appreciate the temperature's relaxation towards the (excitation-free) steady value of ~ 4.23 K within $t = t_0$. Strikingly, for $t > t_0$, a local exponential growth of the temperature is observed in correspondence to the breather, leading to a persisting double-peaked local heating, with $\max\{T_2\} \gtrsim 4.27$ K. Such a profile is a natural consequence of the breather being a two-soliton bound state. A clear thermal fingerprint for the breather is thus brought to light. The latter mode is indeed notoriously hard to track via mean voltage measurements due to its fast (zero-averaging) oscillations, and the few proposals currently available in the literature resort to the breather's destruction for probing purposes [41,43,46]. By virtue of the characteristic '$\cos\varphi$' dependence in Eq. (4), the breather's influence within the thermal realm is nonvanishing, and the detection does not require its breakup—a fact which makes this framework particularly appealing.

It follows from the analytical SG breather solution, see Eq. (5), that the mode's morphology, *e.g.*, its oscillation amplitude and width, encodes information on the breathing frequency [39,40]. It is hence reasonable to expect differently shaped thermal profiles for distinct frequencies, with lower ω values yielding more pronounced double-peaked patterns (since the corresponding breathers are closer to unbound kink–antikink pairs). This is confirmed in Fig. 3(a)–(c), which displays three stationary temperature curves ($T_{2,s}$) at different breather frequencies. Here, the green, blue, and purple lines are obtained, respectively, for $\omega = \{0.3, 0.5, 0.7\}$ and $\eta = \{0.3, 0.33, 0.31\}$, where $\eta \approx \eta_{\rm th}(\omega)$. Note that in the low-frequency representative case a markedly double-peaked waveform emerges, with $\max\{T_{2,s}\} \gtrsim 4.27$ K, while in the high-frequency one the resulting curve is essentially bell-shaped, with $\max\{T_{2,s}\} \lesssim 4.27$ K. The result at $\omega = 0.5$ is somewhat

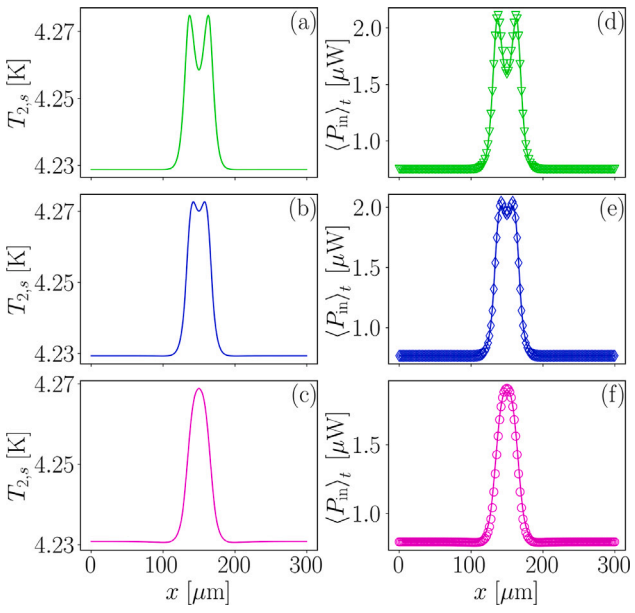

Fig. 3. Panels (a)–(c): Stationary temperature curves ($T_{2,s}$) at different breather frequencies. Panels (d)–(f): Time-averaged thermal powers $\langle P_{\rm in}\rangle_t$ corresponding to the simulations from panels (a)–(c) (lines) and their analytical counterparts, *i.e.*, $\left\langle P_{\rm in}(T_1, T_b, \varphi^0, V^0)\right\rangle_t$ (triangles, diamonds, and circles). In the panels, $\Gamma = 0$ is set, and the green, blue, and purple colors stand for the combinations $\omega = 0.3$ and $\eta = 0.3$, $\omega = 0.5$ and $\eta = 0.33$, and $\omega = 0.7$ and $\eta = 0.31$, respectively. (For interpretation of the references to color in this figure legend, the reader is referred to the web version of this article.)

in between the previous two, as one may guess. Far from electrode's center, $T_{2,s} \sim 4.23$ K is obtained in all scenarios.

As hinted above, the temperature's envelope reflects the behavior of the thermal power $P_{\rm in}$. This structural analogy is clearly demonstrated through Fig. 3(d)–(f), where the lines indicate the time-averaged thermal powers $\langle P_{\rm in}\rangle_t$[5] relative to the simulations of Eqs. (1) and (3) discussed in panels (a)–(c). In particular, the local enhancement of the average thermal power is higher for the prominent double-peaked (green) profile, for which $\max\{\langle P_{\rm in}\rangle_t\} \gtrsim 2$ μW, whereas the bell-shaped (purple) one is characterized by $\max\{\langle P_{\rm in}\rangle_t\} \lesssim 2$ μW. The $\omega = 0.5$ (blue) outcome falls once again in between the prior two. In all cases, $\langle P_{\rm in}\rangle_t \lesssim 1$ μW is observed away from the breather.

Fig. 3(d)–(f) features also a comparison between the above mentioned $\langle P_{\rm in}\rangle_t$ curves and their analytical counterparts. More specifically, the green triangles ($\omega = 0.3$), the blue diamonds ($\omega = 0.5$), and the purple circles ($\omega = 0.7$) are calculated directly from Eq. (5) as $\left\langle P_{\rm in}(T_1, T_b, \varphi^0, V^0)\right\rangle_t$, with $V^0 = [\Phi_0/(2\pi)]\left(\partial\varphi^0/\partial t\right)$ being the voltage profile associated to φ^0, without using Eqs. (1) and (3). The great accordance displayed is yet another indication that the unveiled phenomenology can be rigorously ascribed to the breather waveform.

Detection proposal. Pairing the revealed thermal fingerprint with a reliable breather excitation and stabilization technique is an important task in view of an experimental detection. To this end, it has been recently established that, starting from the realistic $\varphi = 0$ initial condition, the combination of noise and ac forcing can lead to the emergence of long-time stable breather modes in random locations [46,47].

In the simulation shown in Fig. 4, the noisy junction ($\Gamma = 0.0026$, see Section 2) is driven with the frequency/amplitude combination $\omega = 0.6$ and $\eta = 0.59$ [46,47]. After the excitation-free thermalization of the electrode S_2 for $t < t_0$, a noise-induced and ac-locked breather

[5] The time average is intended for $t \geq t_0$, with the simulations' being performed in analogous fashion to that presented in Fig. 2.

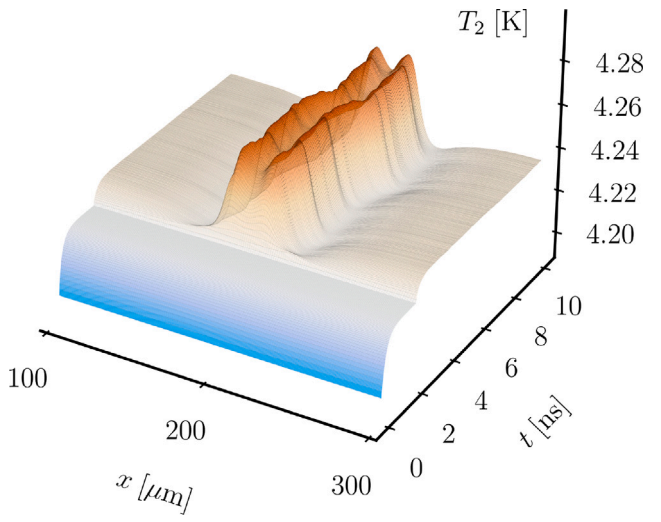

Fig. 4. Spatio-temporal view of the temperature T_2. A noise-induced and ac-locked breather, centered roughly at 200 μm, is observed for $t \gtrsim t_0 = 2$ ns, *i.e.*, after S_2's thermalization at the steady value of ~ 4.23 K has occurred. Focusing on the region $[100, 300]$ μm, the breather is shown to induce a double-peaked local heating, with $\max\{T_2\} \gtrsim 4.27$ K. Parameter values: $\omega = 0.6$, $\eta = 0.59$, and $\Gamma = 0.0026$.

arises close to 200 μm, which motivates the plot's focus on the region $[100, 300]$ μm. Interestingly, the distinctive traits of the breather's influence on the temperature T_2 are preserved even in the stochastic scenario. As one expects, now the position of the solitonic state's center slightly fluctuates in time, along with its amplitude, but the overall behavior is analogous to that presented in Fig. 2. A double-peaked local heating, with $\max\{T_2\} \gtrsim 4.27$ K, is indeed clearly seen.

To experimentally capture the above profile, one may estimate the need for a resolution in the temperature measurements around 10 mK, which can be achieved within present-day Josephson setups [3,5,72,73], as well as a spatial resolution of the order of 10 μm. Furthermore, while simulating Eqs. (1) and (3) over timescales greater than $t_f = 10$ ns is technically challenging (see Appendix B), the latter should not be intended as a time resolution requirement for experiments, and the discussed effects already show robustness over thousands of breathing cycles. Also, it may be desirable to work with a smaller forcing frequency. As shown in Fig. 3(a), reducing ω enhances the double-peaked feature of the thermal profile because the kink–antikink couple forming the breather is bound less tightly than in the higher frequency case. Another viable option may be to lower the plasma frequency ω_p, since Nb/Al–AlO_x/Nb junctions with $\omega_p/2\pi \sim 10$ GHz can be fabricated [74].

The present discussion identifies, under realistic conditions, the key ingredients for a successful breather detection scheme which, notably, does not require the mode's destruction. In this regard, noisy and ac-driven LJJs are identified as natural candidates for unveiling the breather's thermal fingerprint.

4. Conclusions

It is demonstrated that SG breathers enhance the heat transfer in thermally biased, overlap-geometry LJJs. This brings to light a soliton-based mechanism for mastering the local temperature within the system. Another important point is that this effect allows for the design of a non-destructive breather detection strategy. Notably, distinct breathing frequencies yield morphologically different local temperature peaks, which are well understood in terms of the analytical SG breather profile and can be experimentally identified. To illustrate the robustness of the results, the present work pairs the above thermal fingerprint with a reliable technique of breather generation and stabilization, via the combined action of noise and ac driving [46,47]. In other words, we provide an experimental blueprint for the generation and detection of breathers in noisy and ac-driven LJJs within reach of current technology.

Another feasible approach for detecting breathers in LJJs may be a thermal quench [75], which can also be studied in detail within our framework, and thus represents an interesting direction for future research. Furthermore, we note that inhomogeneous bias current distributions, naturally occurring in LJJs [76–78], can determine where stabilized breathers may be located within the junction [79], a fact which surely helps in optimally placing the thermometers in a concrete detection experiment.

Extensive literature has also focused on creating and controlling Josephson vortices in LJJs based on normal metal [80–84]. Considering that SG frameworks are often employed in this context as well [81], it may be interesting to investigate the interplay between thermal and solitonic effects in a fashion similar to that presented here.

The developed ideas are expected to find application even beyond the LJJ device. In particular, it seems reasonable to look at discrete systems, and exploit a similar approach to study and probe, for example, the elusive oscillobreather states in parallel arrays of thermally biased superconducting junctions [85]. Moreover, a connection between the present scenario and the more general context of soliton-sustained heat propagation in various devices, such as wires and nanotubes [86,87], naturally comes to mind.

CRediT authorship contribution statement

Duilio De Santis: Writing – review & editing, Writing – original draft, Visualization, Validation, Software, Resources, Methodology, Investigation, Formal analysis, Data curation, Conceptualization. **Bernardo Spagnolo:** Writing – review & editing, Validation, Methodology, Investigation, Funding acquisition, Formal analysis. **Angelo Carollo:** Writing – review & editing, Validation, Investigation, Formal analysis. **Davide Valenti:** Writing – review & editing, Validation, Supervision, Project administration, Methodology, Investigation, Funding acquisition, Formal analysis. **Claudio Guarcello:** Writing – review & editing, Validation, Supervision, Software, Methodology, Investigation, Formal analysis, Data curation.

Declaration of competing interest

The authors declare that they have no known competing financial interests or personal relationships that could have appeared to influence the work reported in this paper.

Data availability

Data will be made available on request.

Acknowledgments

The authors acknowledge the support of the Italian Ministry of University and Research (MUR).

Appendix A. Modeling of the thermally biased long Josephson junction

To model the evolution of the floating temperature, one should discuss the typical length scale for thermalization within the electrode. In the diffusive regime, the inelastic scattering length can be considered $l_{\rm in} = \sqrt{\tau_s \mathcal{D}} \approx 0.3$ μm for Nb at 4.2 K, where τ_s is the quasiparticle scattering lifetime and $\mathcal{D} = \sigma_N / \left(e^2 N_F\right)$ is the diffusion constant, with σ_N and N_F being, respectively, the electrical conductivity in the normal state and the density of states at the Fermi energy (e is the electron charge). Since exclusively the junction length L is much larger than $l_{\rm in}$, S_2 essentially behaves as a 1-D diffusive superconductor, and Eq. (3)

holds [36]. Furthermore, in Eq. (3), the electronic heat conductivity $\kappa(T_2)$ reads [68]

$$\kappa(T_2) = \frac{\sigma_N}{2e^2 k_B T_2^2} \int_{-\infty}^{+\infty} \varepsilon^2 \frac{\cos^2\left\{\mathrm{Im}\left[\mathrm{arctanh}\left(\frac{\Delta(T_2)}{\varepsilon+i\gamma}\right)\right]\right\}}{\cosh^2\left(\frac{\varepsilon}{2k_B T_2}\right)} d\varepsilon. \tag{A.1}$$

Here, the BCS-like superconducting gap $\Delta(T) = \Delta \tanh\left(1.74\sqrt{T_c/T-1}\right)$ is employed [88], with $\Delta = 1.764 k_B T_c$, $T_c = 9.2$ K being the critical temperature for Nb, and $\gamma = 10^{-4}\Delta$ the Dynes broadening parameter [89].

In the adiabatic limit, *i.e.*, when $eV \ll \min\left\{k_B T_1, k_B T_2, \Delta(T_1), \Delta(T_2)\right\}$, one can write [70]

$$\mathcal{P}_{\mathrm{qp}}(T_1,T_2,V) = \frac{1}{e^2 R_a d_2} \int_{-\infty}^{+\infty} \mathcal{N}(\varepsilon - eV, T_1)\mathcal{N}(\varepsilon, T_2)\times \\ \times (\varepsilon - eV)\left[f(\varepsilon - eV, T_1) - f(\varepsilon, T_2)\right] d\varepsilon \tag{A.2}$$

and

$$\mathcal{P}_{\cos}(T_1,T_2,V) = \frac{1}{e^2 R_a d_2} \int_{-\infty}^{\infty} \mathcal{N}(\varepsilon - eV, T_1)\mathcal{N}(\varepsilon, T_2)\times \\ \times \frac{\Delta(T_1)\Delta(T_2)}{\varepsilon}\left[f(\varepsilon - eV, T_1) - f(\varepsilon, T_2)\right] d\varepsilon, \tag{A.3}$$

in which $\mathcal{N}(\varepsilon,T) = \left|\mathrm{Re}\left[\frac{\varepsilon+i\gamma}{\sqrt{(\varepsilon+i\gamma)^2-\Delta(T)^2}}\right]\right|$ is the reduced superconducting density of state, and $f(\varepsilon,T) = \left[1+e^{\varepsilon/(k_B T)}\right]^{-1}$ is the Fermi distribution function. The breather oscillations quickly average to zero voltage, *i.e.*, $\langle V_b\rangle_t \approx 0$ is observed over times much smaller than the characteristic time of Eq. (3), thus satisfying the above adiabatic condition. Furthermore, it should be emphasized that the essence of the phenomenology, that is, the thermal profiles discussed in the main text (Figs. 2–4), lies in the cosine φ-dependence alone.

The 'e-ph' thermal power density accounts for the energy exchange between electrons and phonons in the superconductor, and it is given by [67]

$$\mathcal{P}_{\mathrm{e-ph}} = \frac{-\Sigma}{96\zeta(5)k_B^5} \int_{-\infty}^{\infty} E dE \int_{-\infty}^{\infty} \varepsilon^2 \mathrm{sign}(\varepsilon) M_{E,E+\varepsilon} \left\{\coth\left(\frac{\varepsilon}{2k_B T_b}\right)\right. \\ \left.\times\left[\mathcal{F}(E,T_2) - \mathcal{F}(E+\varepsilon,T_2)\right] - \mathcal{F}(E,T_2)\mathcal{F}(E+\varepsilon,T_2) + 1\right\} d\varepsilon, \tag{A.4}$$

where Σ is the electron–phonon coupling constant, ζ is the Riemann zeta function, $M_{E,E'} = \mathcal{N}(E,T_2)\mathcal{N}(E',T_2)\left[1-\Delta(T_2)^2/\left(EE'\right)\right]$, and $\mathcal{F}(\varepsilon,T_2) = \tanh\left[\varepsilon/\left(2k_B T_2\right)\right]$. Here, the lattice phonons of the superconductor are assumed to be thermalized with the substrate residing at T_b by virtue of the vanishing Kapitza resistance between the thin metallic films and the substrate at low temperatures [2].

The RHS of Eq. (3) involves $c_v(T_2) = T_2\left(dS/dT_2\right)$, which is defined in terms of the electronic entropy density of S_2 [14]

$$S(T_2) = -4k_B N_F \int_0^{+\infty} \mathcal{N}(\varepsilon,T_2)\times \\ \times\left\{\left[1-f(\varepsilon,T_2)\right]\ln\left[1-f(\varepsilon,T_2)\right] + f(\varepsilon,T_2)\ln f(\varepsilon,T_2)\right\} d\varepsilon. \tag{A.5}$$

The following parameter values are considered: $\sigma_N = 6.7\times 10^6\ \Omega^{-1}\ \mathrm{m}^{-1}$, $N_F = 10^{47}\ \mathrm{J}^{-1}\ \mathrm{m}^{-3}$, and $\Sigma = 3\times 10^9\ \mathrm{W\ m^{-3}\ K^{-5}}$.

To conclude, it is perhaps worth mentioning that the present framework can be rephrased to apply for junctions involving non-identical electrodes as well.

Appendix B. Numerical details

Implicit finite-difference schemes are used to solve both the perturbed SG equation and the diffusion equation, keeping the same spatio-temporal grid in the two cases. In particular, the spatial domain is divided into $\mathcal{N}$ cells of length Δx and the temporal domain into $\mathcal{M}$ intervals of duration Δt. The perturbed SG equation is handled in the same way as in Ref. [46], see its Supplemental Material for a complete account of this matter. In Eq. (3), indicating the space–time restriction of $T_2(x,t)$ as $(T_2)_n^m = T_2(n\,\Delta x, m\,\Delta t)$, for $n = 1,\dots,\mathcal{N}$ and $m = 1,\dots,\mathcal{M}$, the derivatives are [90]

$$\frac{\partial T_2}{\partial x} \approx \frac{1}{2\Delta x}\left[(T_2)_{n+1}^m - (T_2)_{n-1}^m\right], \\ \frac{\partial T_2}{\partial t} \approx \frac{1}{\Delta t}\left[(T_2)_n^{m+1} - (T_2)_n^m\right], \\ \frac{\partial^2 T_2}{\partial x^2} \approx \frac{1}{2\Delta x^2}\left[(T_2)_{n+1}^{m+1} - 2(T_2)_n^{m+1} + (T_2)_{n-1}^{m+1} + \right. \\ \left. +(T_2)_{n+1}^m - 2(T_2)_n^m + (T_2)_{n-1}^m\right]. \tag{B.1}$$

By also applying both the initial and the boundary conditions, a tridiagonal system of equations is obtained. The latter's resolution, achievable through, *e.g.*, the Thomas' algorithm [91], determines the unknown values $(T_2)_n^{m+1}$, given the previous ones $(T_2)_n^m$, with $n = 1,\dots,\mathcal{N}$. Throughout the work, the values of the discretization steps are $\Delta x = 0.4$ μm and $\Delta t = 0.01$ ps (*i.e.*, $\Delta\mathcal{X} = \Delta x/\lambda_J = 0.05$ and $\Delta\mathcal{T} = \Delta t\,\omega_p = 0.01$).

There is one more technical aspect concerning the solution of Eq. (3), that is, the T_2-dependent integrals in Eqs. (A.1)–(A.5). At each time step of the implicit scheme, in principle, one would need to numerically compute the latter objects by using the instantaneous T_2 temperature profile [note that Eqs. (A.2)–(A.3) also depend on the instantaneous voltage]. Given the time-consuming nature of this task, another approach is pursued here. Via preliminary testing, very refined grids covering the entire variation range of the required quantities, *i.e.*, T_2 and V, are constructed to evaluate all the integrals beforehand. These results are stored, and subsequently (if needed) standard interpolation routines are called to fill the gaps. The use of `scipy`'s `integrate.quad` (which is based on the `Fortran` library `QUADPACK`), as well as its interpolation schedules, is acknowledged.

Appendix C. Parameter values for the sine–Gordon model in the thermally biased scenario

The parameters introduced within the SG framework are influenced by the temperatures T_1 and T_2, and therefore they must be set properly. In particular, the effective magnetic thickness is given by [8]

$$t_d(T_1,T_2) = \lambda_L(T_1)\tanh\left[\frac{d_1}{2\lambda_L(T_1)}\right] + \lambda_L(T_2)\tanh\left[\frac{d_2}{2\lambda_L(T_2)}\right] + d, \tag{C.1}$$

where $\lambda_L(T) = \frac{\lambda_L^0}{\sqrt{1-(T/T_c)^4}}$ is the London penetration depth, and d_i is the thickness of the electrode S_i. The above assumption of a fixed temperature T_1 amounts to consider a very large S_1 volume, thus $d_1 \gg \lambda_L(T_1)$ is taken, which yields

$$t_d(T_1,T_2) \approx \lambda_L(T_1) + \lambda_L(T_2)\tanh\left[\frac{d_2}{2\lambda_L(T_2)}\right] + d. \tag{C.2}$$

Moreover, the Ambegaokar–Baratoff relation holds for the Josephson critical current

$$I_c(T_1,T_2) = \frac{1}{2eR}\left|\int_{-\infty}^{\infty}\left\{\mathcal{F}(\varepsilon,T_1)\mathrm{Re}\left[\mathfrak{F}(\varepsilon,T_1)\right]\mathrm{Im}\left[\mathfrak{F}(\varepsilon,T_2)\right] + \right.\right. \\ \left.\left. +\mathcal{F}(\varepsilon,T_2)\mathrm{Re}\left[\mathfrak{F}(\varepsilon,T_2)\right]\mathrm{Im}\left[\mathfrak{F}(\varepsilon,T_1)\right]\right\} d\varepsilon\right|, \tag{C.3}$$

in which $R = R_a/A$ is the normal resistance, and $\mathfrak{F}(\varepsilon,T) = \frac{\Delta(T)}{\sqrt{(\varepsilon+i\gamma)^2-\Delta(T)^2}}$ is the anomalous Green's function [12]. As a result, one gets the Josephson penetration depth $\lambda_J(T_1,T_2) = \sqrt{\Phi_0/\left[2\pi\mu_0 t_d(T_1,T_2)J_c(T_1,T_2)\right]}$, the normalized junction length $\mathcal{L}(T_1,T_2) = L/\lambda_J(T_1,T_2)$, the Josephson plasma frequency $\omega_p(T_1,T_2) = \sqrt{2\pi J_c(T_1,T_2)/\left(\Phi_0 C\right)}$, the dissipation coefficient $\alpha(T_1,T_2) = 1/\left[\omega_p(T_1,T_2)R_a C\right]$, and the noise strength $\Gamma(T_1,T_2) = 2\pi\mathcal{L}(T_1,T_2)k_B T_1/\left[\Phi_0 I_c(T_1,T_2)\right]$. Regarding the latter

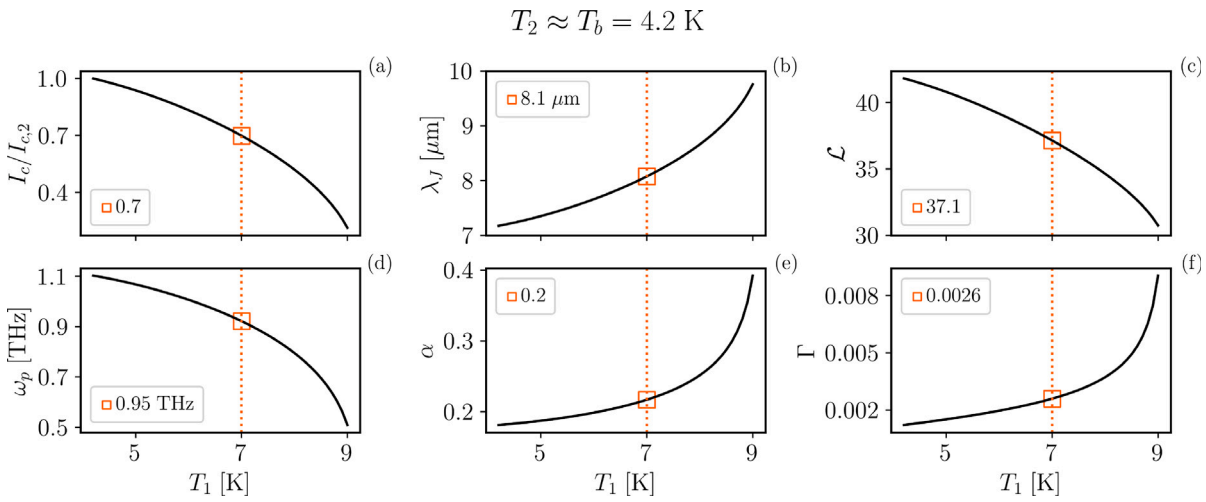

Fig. C.5. Josephson critical current I_c in units of $I_{c,2} = I_c(T_2, T_2)$ [panel (a)], Josephson penetration depth λ_J [panel (b)], normalized junction length $\mathcal{L}$ [panel (c)], Josephson plasma frequency ω_p [panel (d)], dissipation coefficient α [panel (e)], and noise strength Γ [panel (f)] as a function of the temperature T_1. Here, the approximation $T_2 = T_b = 4.2$ K is used, and the orange squares denote the parameter values at $T_1 = 7$ K, *i.e.*, those employed throughout the work.

quantity, the explicit T_1 in the numerator indicates that the 'worst-case' noise scenario is being accounted for.

Using the approximation $T_2 = T_b = 4.2$ K (since T_2's variations discussed in the paper are negligible for the present purpose), Fig. C.5 displays I_c in units of $I_{c,2} = I_c(T_2, T_2)$ [panel (a)], λ_J [panel (b)], $\mathcal{L}$ [panel (c)], ω_p [panel (d)], α [panel (e)], and Γ [panel (f)] versus the temperature T_1. The orange squares denote the parameter values at $T_1 = 7$ K, *i.e.*, those employed throughout the work. Note also that, in addition to those listed above, the value $\lambda_L^0 = 80$ nm is assumed here.

References

[1] Pekola JP. Towards quantum thermodynamics in electronic circuits. Nat Phys 2015;11:118–23.

[2] Giazotto F, Heikkilä TT, Luukanen A, Savin AM, Pekola JP. Opportunities for mesoscopics in thermometry and refrigeration: Physics and applications. Rev Modern Phys 2006;78:217–74. http://dx.doi.org/10.1103/RevModPhys.78.217.

[3] Pekola JP, Karimi B. Colloquium: Quantum heat transport in condensed matter systems. Rev Modern Phys 2021;93:041001. http://dx.doi.org/10.1103/RevModPhys.93.041001.

[4] Martínez-Pérez MJ, Solinas P, Giazotto F. Coherent caloritronics in Josephson-based nanocircuits. J Low Temp Phys 2014;175:813–37. http://dx.doi.org/10.1007/s10909-014-1132-6.

[5] Fornieri A, Giazotto F. Towards phase-coherent caloritronics in superconducting circuits. Nat Nanotechnol 2017;12:944–52. http://dx.doi.org/10.1038/nnano.2017.204.

[6] Hwang SY, Sothmann B. Phase-coherent caloritronics with ordinary and topological Josephson junctions. Eur Phys J: Spec Top 2020;229:683–705. http://dx.doi.org/10.1140/epjst/e2019-900094-y.

[7] Giazotto F, Martínez-Pérez MJ. The Josephson heat interferometer. Nature 2012;492:401–5. http://dx.doi.org/10.1038/nature11702.

[8] José Martínez-Pérez M, Giazotto F. A quantum diffractor for thermal flux. Nat Commun 2014;5:3579.

[9] Kuzmin L. Ultra-sensitive cryogenic thermometer based on an array of the SIN tunnel junctions. Physica C 2008;468:142–6. http://dx.doi.org/10.1016/j.physc.2007.10.024.

[10] Giazotto F, Solinas P, Braggio A, Bergeret FS. Ferromagnetic-insulator-based superconducting junctions as sensitive electron thermometers. Phys Rev Appl 2015;4:044016. http://dx.doi.org/10.1103/PhysRevApplied.4.044016.

[11] Zgirski M, Foltyn M, Savin A, Norowski K, Meschke M, Pekola J. Nanosecond thermometry with Josephson junctions. Phys Rev Appl 2018;10:044068. http://dx.doi.org/10.1103/PhysRevApplied.10.044068.

[12] Guarcello C, Braggio A, Solinas P, Giazotto F. Nonlinear critical-current thermal response of an asymmetric Josephson tunnel junction. Phys Rev Appl 2019;11:024002. http://dx.doi.org/10.1103/PhysRevApplied.11.024002.

[13] Hofer PP, Perarnau-Llobet M, Brask JB, Silva R, Huber M, Brunner N. Autonomous quantum refrigerator in a circuit QED architecture based on a Josephson junction. Phys Rev B 2016;94:235420. http://dx.doi.org/10.1103/PhysRevB.94.235420.

[14] Solinas P, Bosisio R, Giazotto F. Microwave quantum refrigeration based on the Josephson effect. Phys Rev B 2016;93:224521. http://dx.doi.org/10.1103/PhysRevB.93.224521.

[15] Gordeeva AV, Zbrozhek VO, Pankratov AL, Revin LS, Shamporov VA, Gunbina AA, et al. Observation of photon noise by cold-electron bolometers. Appl Phys Lett 2017;110:162603. http://dx.doi.org/10.1063/1.4982031.

[16] Gordeeva A, Pankratov A, Pugach N, Vasenko A, Zbrozhek V, Blagodatkin A, et al. Record electron self-cooling in cold-electron bolometers with a hybrid superconductor-ferromagnetic nanoabsorber and traps. Sci Rep 2020;10:21961.

[17] Hwang SY, Sothmann B, Sánchez D. Superconductor–quantum dot hybrid coolers. Phys Rev B 2023;107:245412. http://dx.doi.org/10.1103/PhysRevB.107.245412.

[18] Guarcello C, Solinas P, Braggio A, Di Ventra M, Giazotto F. Josephson thermal memory. Phys Rev Appl 2018;9:014021. http://dx.doi.org/10.1103/PhysRevApplied.9.014021.

[19] Ligato N, Paolucci F, Strambini E, Giazotto F. Thermal superconducting quantum interference proximity transistor. Nat Phys 2022;18:627–32. http://dx.doi.org/10.1038/s41567-022-01578-z.

[20] Scharf B, Braggio A, Strambini E, Giazotto F, Hankiewicz EM. Topological Josephson heat engine. Commun Phys 2020;3:198. http://dx.doi.org/10.1038/s42005-020-00463-6.

[21] Cavaliere F, Razzoli L, Carrega M, Benenti G, Sassetti M. Hybrid quantum thermal machines with dynamical couplings. iScience 2023;26. http://dx.doi.org/10.1016/j.isci.2023.106235.

[22] Timossi GF, Fornieri A, Paolucci F, Puglia C, Giazotto F. Phase-tunable Josephson thermal router. Nano Lett 2018;18:1764–9. http://dx.doi.org/10.1021/acs.nanolett.7b04906.

[23] Hwang SY, Giazotto F, Sothmann B. Phase-coherent heat circulator based on multiterminal Josephson junctions. Phys Rev Appl 2018;10:044062. http://dx.doi.org/10.1103/PhysRevApplied.10.044062.

[24] Acciai M, Hajiloo F, Hassler F, Splettstoesser J. Phase-coherent heat circulators with normal or superconducting contacts. Phys Rev B 2021;103:085409. http://dx.doi.org/10.1103/PhysRevB.103.085409.

[25] Sothmann B, Giazotto F, Hankiewicz EM. High-efficiency thermal switch based on topological Josephson junctions. New J Phys 2017;19:023056. http://dx.doi.org/10.1088/1367-2630/aa60d4.

[26] Guarcello C, Giazotto F, Solinas P. Coherent diffraction of thermal currents in long Josephson tunnel junctions. Phys Rev B 2016;94:054522. http://dx.doi.org/10.1103/PhysRevB.94.054522.

[27] Guarcello C, Braggio A, Solinas P, Pepe GP, Giazotto F. Josephson-threshold calorimeter. Phys Rev Appl 2019;11:054074. http://dx.doi.org/10.1103/PhysRevApplied.11.054074.

[28] Paolucci F. Nonlocal superconducting single-photon detector. Phys Rev Appl 2023;20:014003. http://dx.doi.org/10.1103/PhysRevApplied.20.014003.

[29] Barone A, Paternò G. Physics and applications of the Josephson effect. New York: Wiley; 1982.

[30] Mazo JJ, Ustinov AV. The Sine-Gordon equation in Josephson-junction arrays. Springer International Publishing; 2014, p. 155–75. http://dx.doi.org/10.1007/978-3-319-06722-3_7.

[31] Braginski AI. Superconductor electronics: Status and outlook. J Supercond Nov Magn 2019;32:23–44.

[32] Wustmann W, Osborn KD. Reversible fluxon logic: Topological particles allow ballistic gates along one-dimensional paths. Phys Rev B 2020;101:014516. http://dx.doi.org/10.1103/PhysRevB.101.014516.

[33] Wildermuth M, Powalla L, Voss JN, Schön Y, Schneider A, Fistul MV, et al. Fluxons in high-impedance long Josephson junctions. Appl Phys Lett 2022;120:112601.

[34] Lewis RM, Frank MP. Two circuits for directing and controlling ballistic fluxons. IEEE Trans Appl Supercond 2023;33:1–5. http://dx.doi.org/10.1109/TASC.2023.3244115.

[35] Grankin A, Kollár AJ, Hafezi M. Extended josephson junction qubit system. 2023, arXiv preprint arXiv:2309.05212.

[36] Guarcello C, Solinas P, Braggio A, Giazotto F. Solitonic Josephson thermal transport. Phys Rev Appl 2018;9:034014. http://dx.doi.org/10.1103/PhysRevApplied.9.034014.

[37] Guarcello C, Solinas P, Braggio A, Giazotto F. Phase-coherent solitonic Josephson heat oscillator. Sci Rep 2018;8:1–12.

[38] Guarcello C, Solinas P, Giazotto F, Braggio A. Thermal flux-flow regime in long Josephson tunnel junctions. J Stat Mech-Theory E 2019;2019:084006. http://dx.doi.org/10.1088/1742-5468/ab3194.

[39] Scott AC. Nonlinear science: emergence and dynamics of coherent structures. Oxford; 2003.

[40] Dauxois T, Peyrard M. Physics of solitons. Cambridge University Press; 2006.

[41] Gulevich DR, Gaifullin MB, Kusmartsev FV. Controlled dynamics of sine-Gordon breather in long Josephson junctions. Eur Phys J B 2012;85:24.

[42] Monaco R. Traveling electromagnetic waves in annular Josephson tunnel junctions. Wave Motion 2019;88:214–25. http://dx.doi.org/10.1016/j.wavemoti.2019.04.010.

[43] De Santis D, Guarcello C, Spagnolo B, Carollo A, Valenti D. Generation of travelling sine-Gordon breathers in noisy long Josephson junctions. Chaos Solitons Fractals 2022;158:112039. http://dx.doi.org/10.1016/j.chaos.2022.112039.

[44] De Santis D, Guarcello C, Spagnolo B, Carollo A, Valenti D. Supratransmission-induced travelling breathers in long Josephson junctions. Commun Nonlinear Sci Numer Simul 2022;106736. http://dx.doi.org/10.1016/j.cnsns.2022.106736.

[45] De Santis D, Guarcello C, Spagnolo B, Carollo A, Valenti D. Breather dynamics in a stochastic sine-Gordon equation: Evidence of noise-enhanced stability. Chaos Solitons Fractals 2023;168:113115. http://dx.doi.org/10.1016/j.chaos.2023.113115.

[46] De Santis D, Guarcello C, Spagnolo B, Carollo A, Valenti D. Ac-locking of thermally-induced sine-Gordon breathers. Chaos Solitons Fractals 2023;170:113382. http://dx.doi.org/10.1016/j.chaos.2023.113382.

[47] De Santis D, Guarcello C, Spagnolo B, Carollo A, Valenti D. Noise-induced, ac-stabilized sine-Gordon breathers: Emergence and statistics. Commun Nonlinear Sci Numer Simul 2024;131:107796. http://dx.doi.org/10.1016/j.cnsns.2023.107796.

[48] Krasnov VM. Terahertz electromagnetic radiation from intrinsic Josephson junctions at zero magnetic field via breather-type self-oscillations. Phys Rev B 2011;83:174517. http://dx.doi.org/10.1103/PhysRevB.83.174517.

[49] Fujii T, Shibata T, Nishida M, Hatakenaka N. Flying superconducting qubits. IEEE Trans Appl Supercond 2007;17:97–100.

[50] Fujii T, Nishida M, Hatakenaka N. Mobile qubits in quantum Josephson circuits. Phys Rev B 2008;77:024505.

[51] Malomed BA. Soliton models: Traditional and novel, one- and multidimensional. Low Temp Phys 2022;48:856–95. http://dx.doi.org/10.1063/10.0014579.

[52] Chelpanova O, Kelly SP, Morigi G, Schmidt-Kaler F, Marino J. Injection and nucleation of topological defects in the quench dynamics of the Frenkel-Kontorova model. Europhys Lett 2023;143:25002. http://dx.doi.org/10.1209/0295-5075/ace27d.

[53] Ivancevic VG, Ivancevic TT. Sine–Gordon solitons, kinks and breathers as physical models of nonlinear excitations in living cellular structures. J Geom Symmetry Phys 2013;31:1–56.

[54] Dienst A, Casandruc E, Fausti D, Zhang L, Eckstein M, Hoffmann M, et al. Optical excitation of Josephson plasma solitons in a cuprate superconductor. Nat Mater 2013;12:535–41.

[55] Laplace Y, Cavalleri A. Josephson plasmonics in layered superconductors. Adv. Phys.-X 2016;1:387–411. http://dx.doi.org/10.1080/23746149.2016.1212671.

[56] Bykov VG, Trofimenko SV. Slow strain waves in blocky geological media from GPS and seismological observations on the Amurian plate. Nonlinear Process Geophys 2016;23:467–75. http://dx.doi.org/10.5194/npg-23-467-2016.

[57] Žalohar J, Vičič B, Potočnik M, Soklič N, Komac M, Hölscher T, et al. Breather-type oscillations of the global tectonic shear stress fields. J Struct Geol 2020;140:104185. http://dx.doi.org/10.1016/j.jsg.2020.104185.

[58] Hou C, Bu L, Baronio F, Mihalache D, Chen S. Sine–Gordon breathers and formation of extreme waves in self-induced transparency media. Rom Rep Phys 2020;72:405.

[59] Jia M. Bounded states for breathers–soliton and breathers of sine–Gordon equation. Nonlinear Dynam 2021;105:3503–13.

[60] Gritsev V, Polkovnikov A, Demler E. Linear response theory for a pair of coupled one-dimensional condensates of interacting atoms. Phys Rev B 2007;75:174511. http://dx.doi.org/10.1103/PhysRevB.75.174511.

[61] Neuenhahn C, Polkovnikov A, Marquardt F. Localized phase structures growing out of quantum fluctuations in a quench of tunnel-coupled atomic condensates. Phys Rev Lett 2012;109:085304. http://dx.doi.org/10.1103/PhysRevLett.109.085304.

[62] Dalla Torre EG, Demler E, Polkovnikov A. Universal rephasing dynamics after a quantum quench via sudden coupling of two initially independent condensates. Phys Rev Lett 2013;110:090404. http://dx.doi.org/10.1103/PhysRevLett.110.090404.

[63] Lovas I, Citro R, Demler E, Giamarchi T, Knap M, Orignac E. Many-body parametric resonances in the driven sine-Gordon model. Phys Rev B 2022;106:075426. http://dx.doi.org/10.1103/PhysRevB.106.075426.

[64] Horváth DX, Sotiriadis S, Kormos M, Takács G. Inhomogeneous quantum quenches in the sine-Gordon theory. SciPost Phys 2022;12:144. http://dx.doi.org/10.21468/SciPostPhys.12.5.144.

[65] Wybo E, Bastianello A, Aidelsburger M, Bloch I, Knap M. Preparing and analyzing solitons in the Sine–Gordon model with quantum gas microscopes. Phys Rev X Quantum 2023;4:030308. http://dx.doi.org/10.1103/PRXQuantum.4.030308.

[66] Visuri AM. Sine–Gordon dynamics in spin transport. Phys Rev A 2024;109:053310. http://dx.doi.org/10.1103/PhysRevA.109.053310.

[67] Timofeev AV, García CP, Kopnin NB, Savin AM, Meschke M, Giazotto F, et al. Recombination-limited energy relaxation in a bardeen-cooper-schrieffer superconductor. Phys Rev Lett 2009;102:017003. http://dx.doi.org/10.1103/PhysRevLett.102.017003.

[68] Fornieri A, Timossi G, Virtanen P, Solinas P, Giazotto F. 0–π phase-controllable thermal Josephson junction. Nat Nanotechnol 2017;12:425–9.

[69] Maki K, Griffin A. Entropy transport between two superconductors by electron tunneling. Phys Rev Lett 1965;15:921–3. http://dx.doi.org/10.1103/PhysRevLett.15.921, URL https://link.aps.org/doi/10.1103/PhysRevLett.15.921.

[70] Golubev D, Faivre T, Pekola JP. Heat transport through a Josephson junction. Phys Rev B 2013;87:094522. http://dx.doi.org/10.1103/PhysRevB.87.094522.

[71] Lomdahl PS, Samuelsen MR. Persistent breather excitations in an ac-driven sine-Gordon system with loss. Phys Rev A 1986;34:664.

[72] Schmidt D, Yung C, Cleland A. Temporal measurement of hot-electron relaxation in a phonon-cooled metal island. Phys Rev B 2004;69:140301.

[73] Gümüş E, Majidi D, Nikolić D, Raif P, Karimi B, Peltonen JT, et al. Calorimetry of a phase slip in a Josephson junction. Nat Phys 2023;19:196–200.

[74] Fritzsch L, Köhler HJ, Thrum F, Wende G, Meyer HG. Preparation of Nb/Al–AlOx/Nb Josephson junctions with critical current densities down to 1 A/cm2. Physica C 1998;296:319–24.

[75] Gordeeva AV, Pankratov AL. Defect formation in long Josephson junctions. Phys Rev B 2010;81:212504. http://dx.doi.org/10.1103/PhysRevB.81.212504.

[76] Samuelsen MR, Vasenko SA. Influence of the bias current distribution on the static and dynamic properties of long Josephson junctions. J Appl Phys 1985;57:110–2. http://dx.doi.org/10.1063/1.335383.

[77] Pankratov AL. Long Josephson junctions with spatially inhomogeneous driving. Phys Rev B 2002;66:134526. http://dx.doi.org/10.1103/PhysRevB.66.134526.

[78] Revin L, Pankratov A. Detection of bias inhomogeneity in Josephson junctions by switching current distributions. Chaos Solitons Fractals 2021;149:111068. http://dx.doi.org/10.1016/j.chaos.2021.111068.

[79] Grønbech-Jensen N, Malomed BA, Samuelsen MR. Stability of breathers in the ac-driven sine-Gordon system. Phys Lett A 1992;166:347–51. http://dx.doi.org/10.1016/0375-9601(92)90720-7.

[80] Roditchev D, Brun C, Serrier-Garcia L, Cuevas JC, Bessa VHL, Milošević MV, et al. Direct observation of Josephson vortex cores. Nat Phys 2015;11:332–7. http://dx.doi.org/10.1038/nphys3240.

[81] Dremov VV, Grebenchuk SY, Shishkin AG, Baranov DS, Hovhannisyan RA, Skryabina OV, et al. Local Josephson vortex generation and manipulation with a Magnetic Force Microscope. Nat Comm 2019;10:4009. http://dx.doi.org/10.1038/s41467-019-11924-0.

[82] Grebenchuk SY, Hovhannisyan RA, Dremov VV, Shishkin AG, Chichkov VI, Golubov AA, et al. Observation of interacting Josephson vortex chains by magnetic force microscopy. Phys Rev Res 2020;2:023105. http://dx.doi.org/10.1103/PhysRevResearch.2.023105.

[83] Stolyarov VS, Ruzhitskiy V, Hovhannisyan RA, Grebenchuk S, Shishkin AG, Skryabina OV, et al. Revealing Josephson vortex dynamics in proximity junctions below critical current. Nano Lett 2022;22:5715–22. http://dx.doi.org/10.1021/acs.nanolett.2c00647.

[84] Kalashnikov DS, Ruzhitskiy VI, Shishkin AG, Golovchanskiy IA, Kupriyanov MY, Soloviev II, et al. Demonstration of a Josephson vortex-based memory cell with microwave energy-efficient readout. Commun Phys 2024;7:88. http://dx.doi.org/10.1038/s42005-024-01570-4.

[85] Mazo JJ, Orlando TP. Discrete breathers in Josephson arrays. Chaos 2003;13:733–43.

[86] Sciacca M, Alvarez F, Jou D, Bafaluy J. Heat solitons and thermal transfer of information along thin wires. Int J Heat Mass Transfer 2020;155:119809. http://dx.doi.org/10.1016/j.ijheatmasstransfer.2020.119809.

[87] Sciacca M, Carlomagno I, Sellitto A. Thermal solitons in nanotubes. Wave Motion 2022;113:102967. http://dx.doi.org/10.1016/j.wavemoti.2022.102967.

[88] Senapati K, Blamire MG, Barber ZH. Spin-filter Josephson junctions. Nat Mater 2011;10:849–52.

[89] Dynes RC, Narayanamurti V, Garno JP. Direct measurement of quasiparticle-lifetime broadening in a strong-coupled superconductor. Phys Rev Lett 1978;41:1509–12. http://dx.doi.org/10.1103/PhysRevLett.41.1509.

[90] Ames WF. Numerical methods for partial differential equations. Academic Press; 1977.

[91] Press WH, Teukolsky SA, Vetterling WT, Flannery BP. Numerical recipes in fortran 77: the art of scientific computing. Cambridge University Press; 1992.